CHAPTER 1

FROM THE STANDARD MODEL TO THE QUARK-GLUON PLASMA

This chapter provides an introduction to the general concepts that are relevant for the measurement of the Z-boson and J/ψ production in heavy-ion collisions. The standard model which describes the fundamental compositions of the matter and their interactions is introduced. The Quark-Gluon Plasma (QGP) is then presented as a state of matter at very high temperature and energy density. Finally, heavy-ion collisions are introduced as a unique experimental tool to recreate the QGP and some experimental measurements used in order to study it are presented.

1.1 The standard model of particle physics

According to the standard model, the elementary particles listed in Figure 1.1 can be classified as [1] (i) matter particles with half integer spin (fermions), (ii) force-carrier particles that have integer spin (gauge bosons), and (iii) a scalar boson (Higgs boson).

Fermions can be grouped into leptons and quarks. There are three lepton generations that include each a negative electric charged particle (e^-, μ^-, and τ^-) and its

corresponding anti-lepton with a positive electric charge (e^+, μ^+, and τ^+). Similarly, each lepton generation comprises three leptonic neutrinos (ν_e, ν_μ, and ν_τ) and same number of anti-neutrinos ($\bar{\nu_e}$, $\bar{\nu_\mu}$, and $\bar{\nu_\tau}$). On the quark side, there are six flavors with each one containing a quark (q) and a corresponding anti-quark ($\bar{q}$) with an opposite electric charge. The u, c, and t quarks have positive electric charges +2/3 while the d, s, b quarks have negative electric charges (−1/3). In addition to the electric charges, quarks have also color charges that take three values (red, blue or green). In ordinary matter, quarks are confined inside hadrons that can be categorized according to the number of constituent (valence) quarks and anti-quarks. Baryons (e.g protons) are made of three quarks while mesons (e.g pions) are made of one quark and one anti-quark. Recently, hadrons that contain more than three valence quarks were discovered. In particular the tetraquark Z(4430)- $\{c\bar{c}d\bar{u}\}$ was discovered by the Belle experiment [2], and the two pentaquark states $P_c^+(4380)$ and $P_c^+(4450)$ $\{uudc\bar{c}\}$ were discovered by the LHCb [3].

The standard model governs so far three of the four fundamental interactions:

- **The electromagnetic interaction:** fundamental particles that have electric charges (the six charged leptons and the six quarks) can interact electromagnetically by exchanging photons. The theory of Quantum Electro-Dynamics (QED) is the framework to describe this interaction.

- **The weak interaction:** all fermions can interact weakly by the exchange of $W^\pm$ or Z bosons. The weak interaction is $\sim 10^5$ times weaker than the electromagnetic one. The electroweak theory is the framework in which the electromagnetic and the weak interactions are unified.

- **The strong interaction:** particles with color charges, i.e quarks and gluons can strongly interact by exchanging gluons. This interaction is ~100 times stronger than the electromagnetic one. The Quantum Chromo-Dynamics (QCD) is the theoretical framework dedicated to describe this interaction.

In addition to the interactions included in the standard model, **the gravitation force** is applied on all the massive elementary particles.

In the standard model, elementary particles acquire their masses via the interaction with the Higgs field quantized by the Higgs boson which was recently discovered by the two experiments ATLAS [4] and CMS [5] at CERN in 2012.

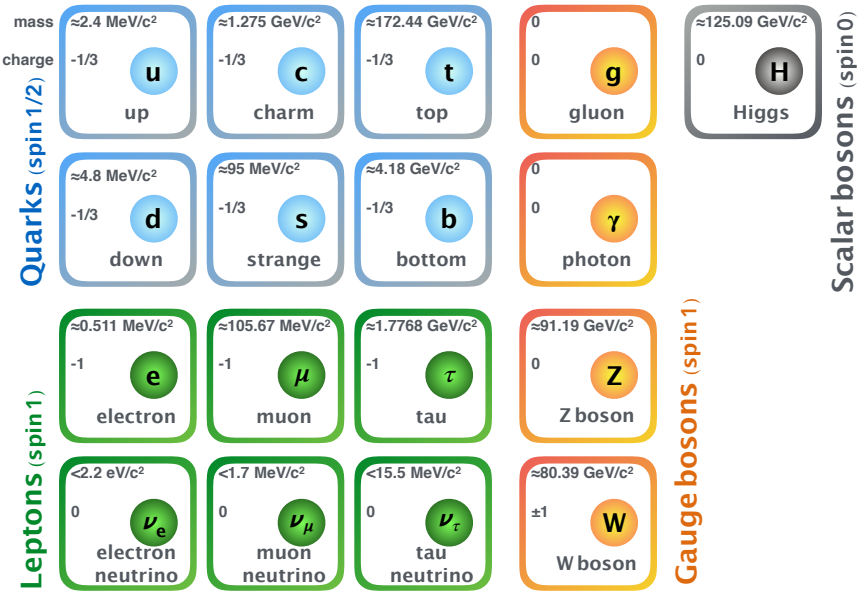

Figure 1.1: Elementary particles discovered at the time of writing this manuscript [1]. For leptons and quarks, the corresponding anti-particles mentioned in the text are not added.

1.1.1 QCD and confinement

In QED, the strength of the coupling between two charged particles decreases with increasing distance (decreasing momentum transfer Q). Indeed, a charged particle (e.g an electron) is screened by virtual e^+e^- pairs from the vacuum, which reduces the effective charge of the particle. If in analogy the QCD vacuum consists only of virtual $q\bar{q}$ pairs, the strength of the strong coupling would behave similarly. However, virtual gluon pairs exist also in this vacuum due to the fact that they have color charges (in contrast to photons which are electrically neutral). The

screening by virtual gluon pairs (known as anti-screening) enhance the effective color charge of the screened particle and consequently causes the coupling to decrease with increasing momentum transfer as shown in Figure 1.2. The strong coupling vanishes when $Q \to \infty$, this is known as asymptotic freedom. In this regime, perturbative QCD calculations are fully valid in describing the strong interaction. At Q values close to the QCD scale ($\Lambda_{QCD} \sim 200MeV$), the coupling constant becomes large and perturbative QCD breaks down. This is the case inside hadrons where the coupling becomes too strong that it is impossible to isolate a quark from a hadron. This mechanism is known as confinement. Lattice QCD (lQCD) is a non-perturbative technique to solve QCD equations. It is based on discretizing the space-time continuum in a finite number of points where the QCD equations can be solved.

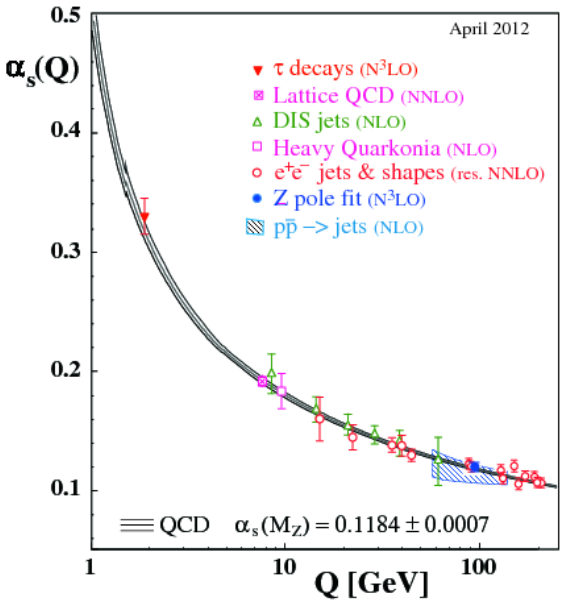

Figure 1.2: Summary of measurements of the strong coupling constant (α_s) as a function of the energy scale Q. Figure is taken from [6].

1.2 Quark-Gluon Plasma

After the big bang, as the universe was expanding and cooling down it undergoes different phase transitions. At a temperature of ~ 10^{16} GeV, the gravity is expected to be separated from the other three fundamental interactions. As the temperature of the universe decreases, the strong and electroweak interactions were separated before the electroweak symmetry breaking took place and the masses of the elementary particles were generated at a temperature of ~ 100 GeV. At this stage, the matter existed as a de-confined medium of quarks and gluons. This state of matter is known as the Quark-Gluon Plasma (QGP). At lower temperature of the order of 100 MeV, the transition between the QGP and the hadronic matter, where the quarks and gluons are confined inside hadrons, is expected to be taken place.

1.2.1 QGP hadron transition

The transition from the de-confined state of matter to the hadronic one is usually characterized in the (T,μ_b) phase space, where T is the temperature and μ_b is the baryo-chemical potential which measures the baryon density of the system. A qualitative phase-space diagram is shown in Figure 1.3. At a given μ_b, the state of matter changes when the temperature reaches a critical value T_c. Latest lQCD calculations [7] predicts $180 < T_c < 200$ MeV at zero μ_b which corresponds to the conditions of the early universe.

The nature of the transition between the de-confined state and the hadronic one across all the phase diagram is still an open question. At zero μ_b, lQCD calculation shows that the transition is a smooth cross-over [8]. However, at $\mu_b \neq 0$, these calculations are still not reliable and theoretical and experimental works are ongoing in order to understand this transition. Calculations from [9] predict the existence of a critical point where the transition becomes a first order transition as shown in Figure 1.3.

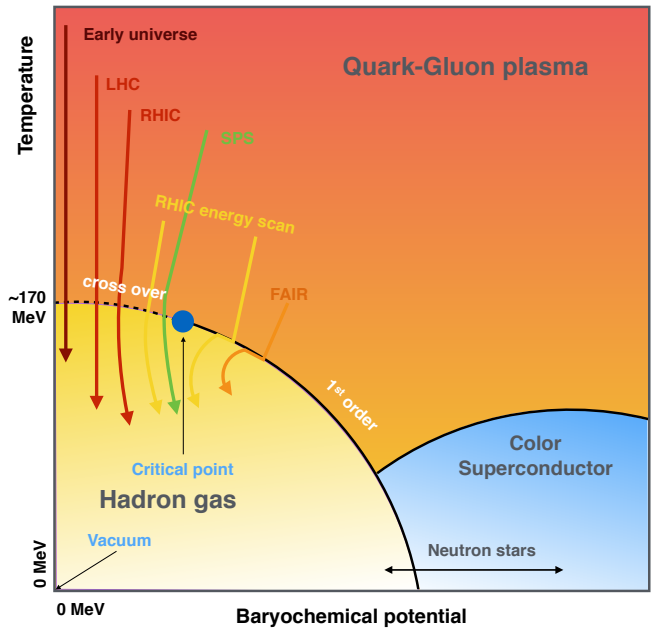

Figure 1.3: A qualitative phase-space diagram characterizing the different states of matter.

1.3 Experimental study of the QGP

By colliding heavy-ion nuclei, the conditions of high energy density and temperature, needed to create the de-confined state of matter, can be reached. Various experimental projects have been established for this purpose. They cover a wide scale of collision energy per nucleon, from ~20 GeV at SPS-CERN, up to 5 TeV at LHC-CERN. With increasing collision energy, T increases while μ_b decreases. This means that the different facilities with different energies probe different (T,μ_b) phase-space regions as also qualitatively indicated in the diagram of Figure 1.3.

1.3.1 Evolution of nuclear collision

In Bjorken picture [10], the evolution of the collision of two heavy nuclei can be schematized by Figure 1.4, where the indicated timescales correspond to a collision at the LHC energies and are not hard numbers but rather rough guidelines according to the Ref [11]. The following stages are listed chronologically:

- In the laboratory frame, the two incoming nuclei are Lorentz contracted. They **cross** each other at a time $\tau_{cross} = 2R/\gamma$, where R is the radius of the nucleus and γ is the Lorentz factor. Scatterings with large momentum transfers between the partons of the nuclei take place at this stage and consequently hard processes (e.g electroweak bosons and heavy flavor quarks) are created.

- In the second stage of the collision, free partons, created from the inelastic collisions of the nucleons of the two nuclei, **thermalize** through additional scatterings. This can lead to the formation of a nuclear matter with high temperature. The system then starts to expand and cools down.

- As the system is cooling down, it reaches a critical temperature where **hadrons** start forming. The **chemical freeze-out** is reached when no further inelastic interactions take place and consequently the number of formed hadrons stays unchanged.

- The formed hadrons gas is still expanding and cooling down until its density is too low that no more elastic collisions take place. The end of this stage is known as **kinetic freeze-out** where the momenta of the formed hadrons are set.

1.3.2 Geometry of nuclear collision

The idea of colliding heavy ions in order to recreate the QGP is essentially based on the large number of involved nucleon-nucleon collisions. Therefore, these conditions may differ depending on the geometry of the initial configuration of the collided nuclei. For instance, the closer the collision is to 'head-on' (more central), the more likely the QGP formation will be. The physical observable that can characterize the initial geometry is the impact parameter (b) which for a hadronic collision can take values from 0 to the sum of the radii of the two nuclei (R_1+R_2).

The number of participating nucleons that undergo at least one inelastic collisions (N_{part}) and the number of binary nucleon-nucleon collision (N_{coll}) can be obtained using Glauber model [12]. It is a model that treats the nucleus-nucleus collision as a superposition of many independent nucleon-nucleon collisions. In

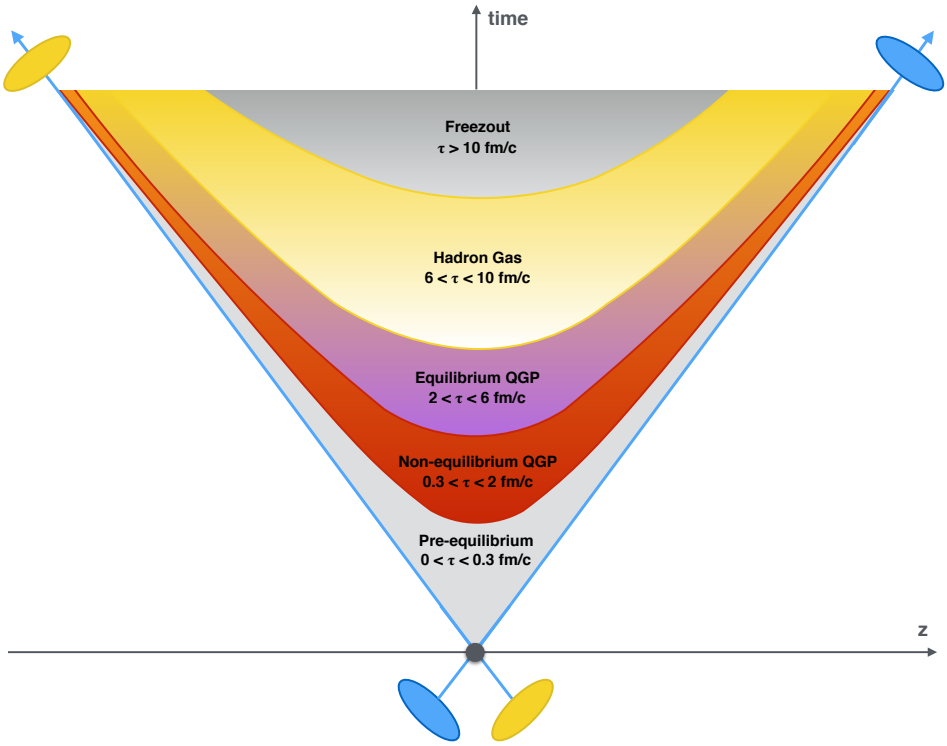

Figure 1.4: Space-time evolution of the collision of two heavy ions. The timescales correspond to a collision at the LHC energies. Figure is taken from [11].

Figure 1.5, two heavy ions A and B collide along the z-direction with an impact parameter b. If one considers the flux tube (red colored surface) located at a transverse distance s from the center of the nucleus A, the probability for a given nucleon to be located in this tube is given by:

$$T_A(s) = \int dz \rho(s,z), \tag{1.1}$$

where $\rho(s,z)$ is the nucleus density distribution. Similar probability is given for the flux tube located at a distance $(s-b)$ from the center of the nucleus B. For a given b, one can define the nuclear overlap function for A-B collision by:

$$T_{AB}(b) = \int d^2 s T_A(s) T_B(s-b). \tag{1.2}$$

$T_{AB}(b)$ can be interpreted as the effective overlap area for which a specific

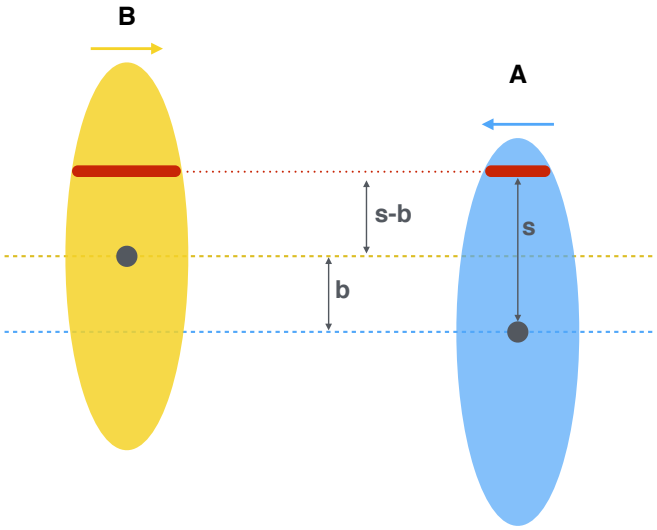

Figure 1.5: Schematic view of the initial geometry of two collided ions A and B separated by an impact parameter b. Figure is taken from [12].

nucleon in A can interact with a given nucleon in B. If σ_{inel}^{NN} is the inelastic nucleon-nucleon cross section, then N_{coll} is expressed as:

$$N_{\text{coll}}(b) = A_A \cdot A_B \sigma_{inel}^{NN} T_{AB}(b), \tag{1.3}$$

where A_A and A_B are respectively the number of nucleons in the nucleus A and B. While N_{part} is given by:

$$N_{\text{part}}(b) = A_A \cdot \int d^2s T_A \left(1 - \left[1 - \sigma_{inel}^{NN} T_B(b-s)\right]^B\right) + B_B \cdot \int d^2s T_B \left(1 - \left[1 - \sigma_{inel}^{NN} T_A(s)\right]^A\right). \tag{1.4}$$

In heavy-ion experiments, the centrality classes and the related quantities ($\langle N_{\text{part}} \rangle$, $\langle N_{\text{coll}} \rangle$, and $\langle T_{\text{AA}} \rangle$) are usually obtained by performing Monte Carlo simulations based on Glauber model of a given measurable quantity (e.g the charged particle multiplicity) and fitting it to real data.

1.4 Probing the QGP

It is not possible experimentally to directly observe the QGP due to its brief lifetime. Therefore, only indirect observations using different signatures to probe the QGP are possible. The different probes can be classified based on the involved momentum scales. Soft probes are those with relatively low momentum transfer and consequently can be created in different stages of the collision. In contrast, hard probes involve large momentum transfer and are consequently created in the early stages of the collisions. In the following, brief descriptions of some of the soft and hard probes are presented. Note that the aim of the following presentation is not to cover all the existed probes but rather to show their variety.

1.4.1 Soft probes

1.4.1.1 Particle yields and ratios

The relative production of hadrons with light (u, d, and s) quarks depend on the state of the system at the chemical freeze-out. Thus measuring the relative yields of different hadrons can be used in order to calculate the temperature of the system at the chemical freeze-out and the baryo-chemical potential. This is usually done by fitting the measured relative yields with statistical models [13].

1.4.1.2 Strangeness enhancement

In hadronic matter, the constituent quarks are dressed with gluons, thus their mass is different than the bare quark mass $m_q \sim 0$. The quark mass is restored in the de-confined matter (this is also known as the chiral symmetry restoration) [14]. As a consequence, the energy threshold of $s\bar{s}$ pair production is smaller in the presence of the QGP. Experimentally, measuring an enhancement of the production of strange hadrons in heavy-ion collisions with respect to what is expected from collisions where no QGP is formed (e.g low multiplicity proton-proton collisions) can be understood as a signature of the QGP formation. Enhanced productions of strange hadrons in heavy-ion collisions have been observed by different experiments [15, 16], [17]. Similarly, an enhancement of strange hadrons has been recently observed in high multiplicity proton-proton collisions [18]. This

is also the case for other measurements in proton-proton collisions (e.g [19, 20]) showing behaviors which are understood to be related to the formation of the QGP.

1.4.1.3 Elliptic flow of charged particles

In non-central heavy-ion collisions, the colliding matter is not symmetrically distributed around the beam axis (almond-shaped). This asymmetry causes, via multiple collisions, an anisotropic momentum distribution as shown in Figure 1.6. For a given particle, the elliptic flow (v_2) is the second order coefficient of the Fourier expansion of the azimuthal distribution of this particle with respect to the reaction plane defined by the beam axis and the impact parameter vector of the colliding nuclei. Measuring the elliptic flow can serve to study the hydrodynamical properties of the expanding medium such that the viscosity and temperature. Other v_n coefficients also exist and have been measured like v_2 by different experiments [21, 22] [23, 24]. They are in general arising from fluctuations of the nucleon positions in the overlap region.

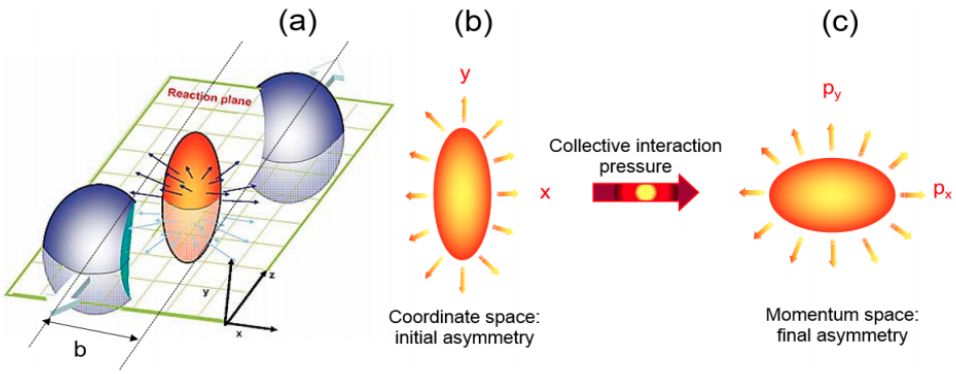

Figure 1.6: (a) A non-central collision of two nuclei leads to an almond-shaped interaction volume; (b) This initial spatial anisotropy with respect to the reaction plane translates via pressure gradients into (c) a momentum anisotropy of the produced particles. Figure is taken from [25].

1.4.2 Hard probes

1.4.2.1 Jet quenching

High energy partons lose energy by radiation when traversing the dense medium via multiple scatterings. This causes the suppression of high transverse momenta particles and known as jet quenching. Experimentally, this can be studied by comparing the yields of high momentum particle in heavy-ion collisions to the same yields measured in proton-proton collisions.

1.4.2.2 Heavy flavor production

Heavy flavor hadrons (contain charm or beauty quarks) and $c\bar{c}$ or $b\bar{b}$ resonances, known respectively as charmonia and bottomonia, are expected to probe the whole phase of the QGP due to the early production of their constituents heavy quarks. Their production can be affected by the presence of the hot medium by energy loss and/or color screening (for quarkonia). Chapter 2 describes the production mechanisms of the charmonium states, and how are used to study different nuclear effects expected to be present in heavy-ion collisions.

1.4.2.3 Electroweak bosons production

The electroweak bosons ($W^{\pm}$ and Z-bosons) are created in the initial hard collisions and do not have color charges thus not affected by the presence of the strongly interacting medium. This makes the study of their production in heavy-ion collisions as clean probes of nuclear effects which are present in the absence of the QGP. In chapter 2, the production of the Z-boson and the different nuclear effects that are relevant to this production are described.

CHAPTER 2

Z-BOSON AND J/ψ PRODUCTION IN HEAVY-ION COLLISIONS

As described in the previous chapter, heavy-ion collisions are the only available experimental tools to produce a strongly interacting medium, QGP. It was discussed that different probes exist to study the created medium, and those probes were classified into two categories, soft and hard depending on their momentum scales.
In this chapter, an overview of the properties and production mechanisms of two hard probes, the Z-boson and the J/ψ is presented. This will be followed by exploring various nuclear effects on the production of the two particles. Finally, a brief overview of the experimental results on Z-boson and J/ψ production in heavy-ion collisions will be given.

2.1 Z-boson hadronic production

The Z-boson is one of the four electroweak gauge bosons (alongside the W^+, the W^-, and the photon). It was discovered at the SPS (CERN) in 1983 [26] and since then has been heavily studied in different experiments [27], [28], [29]. Its intrinsic properties (mass, width, lifetime and couplings), which are among the most precise

measurements in the standard model, were precisely measured by the experiments at the e^+e^- collider LEP [1].Table 2.1 summarizes some of these properties.

		Decay mode fractions		
Mass (GeV)	Width (GeV)	l^+l^-	hadronic	neutrinos
91.1876 ± 0.0021	2.4952 ± 0.0023	(3.3658 ± 0.0023) %	(69.91 ± 0.06) %	(20.00 ± 0.06) %

Table 2.1: Mass, width, and the branching ratios of some decay modes of the Z-boson [1].

The precise knowledge of the mass and the width of the Z-boson makes it a powerful tool for electron and muon energy calibration for particle physics detectors [30]. The Z-boson can also serve as a benchmark for studies and searches for other particles (e.g the Higgs boson) as a known background source.

Theoretically, the Z-boson production in hadronic collisions can be calculated up to NNLO [31]. Figure 2.1 shows examples of leading order (LO), and next-to-leading order (NLO) Feynman diagrams of the Z-boson production. This production is dominated by the LO Drell-Yan (DY)[1] process which is the production of a massive lepton pair via an intermediate Z-boson or an off-mass-shell photon (γ^*) by the annihilation of a quark-antiquark pair. Based on the factorization theorem of hard processes [33], the differential cross section for a DY process in an A-B collision can be expressed as [34]:

$$\sigma_{AB} = \sum_q \frac{4\pi e_q^2 \alpha^2}{9\hat{s}} f_q(x_1, M^2) f_{\bar{q}}(x_2, M^2), \tag{2.1}$$

where $\alpha \approx 1/137$ is the QED coupling constant, e_q is the quark fractional electric charge, $\hat{s} = (p_q + p_{\bar{q}})^2$ is the partonic center-of-mass energy, and $f_{q,\bar{q}}(x, Q^2)$ is the quark (anti-quark) parton distribution functions (PDFs, described in section 2.3.1).

[1] After Sidney D. Drell and Tung-Mow Yan who predicted the process in 1970 [32].

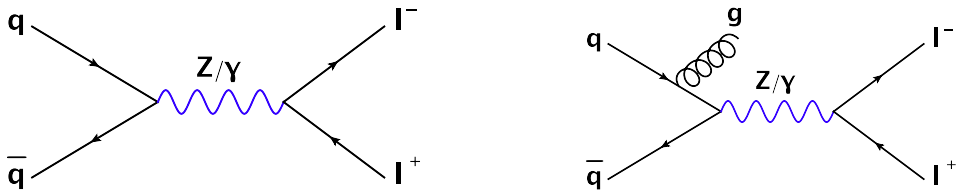

Figure 2.1: Examples of LO (left) and NLO (right) Feynman diagrams of the Z-boson production in hadronic collisions.

2.2 J/ψ properties and production mechanisms

2.2.1 Charmonium states

A charmonium state is a vector meson comprising a charm and an anti-charm quarks. The charmonium mass depends on the angular momentum of the $c\bar{c}$ pair. The spectroscopic notation of a state is given by $n^{2S+1}L_J$ where n,S,L and J are respectively the principal quantum number, the spin, the orbital momentum and the angular momentum of the state. The lowest mass charmonium states correspond to the case where L=0 and they are known as η_c and J/ψ. The latter was the first discovered charmonium state in 1974, simultaneously at SLAC [35] and BNL [36] [2].
The intrinsic properties of different charmonium states are summarized in Table 2.2. In vacuum ($T = 0$), a charmonium bound state, with a separation r between the charm and anti-charm quarks, can be described by a non-relativistic potential due to the large mass of the charm quark [37]

$$V(r, T = 0) = \sigma \cdot r - \frac{\alpha_c}{r}. \tag{2.2}$$

The $1/r$ term in equation 2.2 is Coulomb-like and governs the short distance behavior of the potential. This term represents gluon exchanges between the charm and anti-charm quarks. The coupling factor in the Coulomb-like term, α_c, can be related to the strong coupling constant α_s by a factor that accounts for the summation over color indices, $\alpha_c = (4/3)\alpha_s$ [38]. The linear term corresponds to the

[2] The BNL group gave the new particle the name J while the SLAC group attributed the name ψ.

confining potential obtained from lattice QCD calculations [39], where the string tension σ represents the strength of the confining.

Charmonium	$n^{2S+1}L_J$	mass (MeV/c^2)	width (MeV/c^2)
η_c	1^1S_0	2983.4 ± 0.5	31.8 ± 0.8
J/ψ	1^3S_1	3096.900 ± 0.006	0.0929 ± 0.0028
χ_{c0}	1^3P_0	3414.75 ± 0.31	10.5 ± 0.6
χ_{c1}	1^3P_1	3510.66 ± 0.07	0.84 ± 0.04
h_c	1^1P_1	3525.38 ± 0.11	0.7 ± 0.4
χ_{c2}	1^3P_2	3556.20 ± 0.09	1.93 ± 0.11
$\eta_c(2S)$	2^1S_0	3639.2 ± 1.2	$11.3^{+3.2}_{-2.9}$
ψ(2S)	2^3S_1	3686.097 ± 0.025	0.296 ± 0.008

Table 2.2: Masses and widths of some charmonium states [1].

By emitting photons or pions, heavier charmonium states can decay to lighter ones as shown in Figure 2.2. This is known as charmonium indirect production. In the J/ψ case, this is dominated by the decay of ψ(2S) which has similar quantum numbers as the J/ψ except for the principal quantum number n.

2.2.2 J/ψ hadronic production

Direct and indirect J/ψ productions are both refereed to as prompt production. At the LHC energy, the prompt production is dominated by the gluon fusion mechanism due to the increasing number of the gluons inside the protons with increasing collision energy. However, another J/ψ source is the weak decay of b hadrons. J/ψ from the last source are known as non-prompt. In the following, a brief description of two different models on the prompt J/ψ production, followed by a discussion on the non-prompt one are presented.

2.2.2.1 Color Singlet Model (CSM)

The CSM was proposed shortly after the J/ψ discovery [40]. It is based on the factorization approach to separate the charmonium production cross section into a perturbative and a non-perturbative steps. The former is being the production of

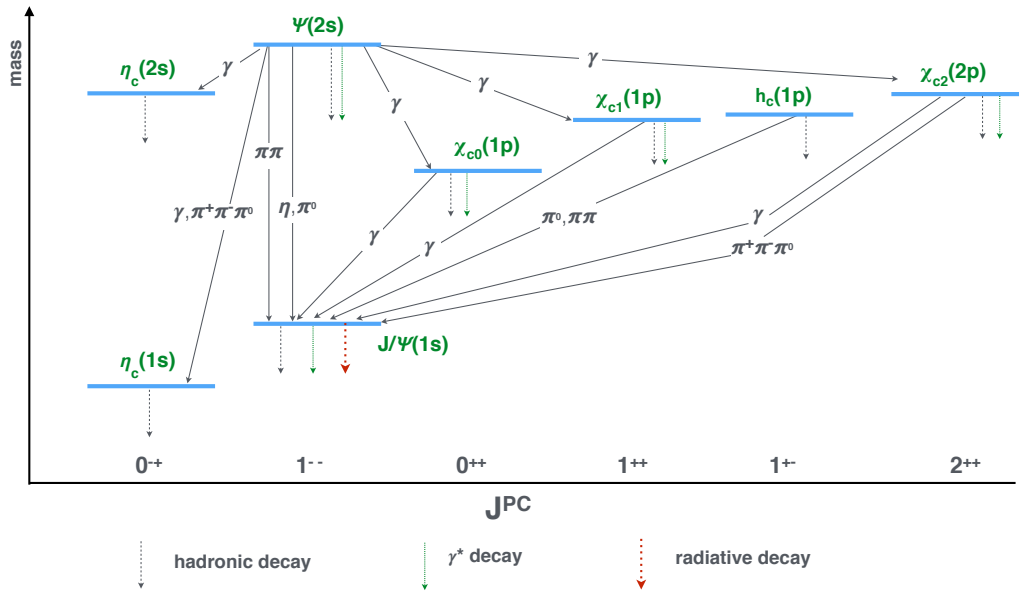

Figure 2.2: Schematic illustration for the different charmonium→charmonium decay channels. Figure is adapted from [1]

on-shell charm and anti-charm quarks, while the latter represents the process of their binding into a charmonium state. During the binding, the model assumes that the charm and anti-charm quarks are at rest in the charmonium frame. Another assumption is that the color charge and the spin of the $c\bar{c}$ pair are unchanged during the whole process, leading to the name of the model since the J/ψ is a color singlet under this assumption.

The strength of the model relies in its prediction power. Indeed, the only free parameters of the model are the absolute values of the color-singlet $c\bar{c}$ wave functions and their derivatives. These wave functions can be determined from data on decay processes or by application of potential models [41].

Predictions made by the CSM have successfully described data at low energy [42]. However, the model underestimates the prompt charmonium production cross section in ppbar collisions at $\sqrt{s}$ = 1.8 TeV at the Tevatron [43] by more than an order of magnitude.

2.2.2.2 Non-Relativistic Quantum Chromo-Dynamics (NRQCD)

This model [44] also factorizes the charmonium production cross section into perturbative and non-perturbative steps, but unlike the CSM, it does not assume that the charm quarks are produced in their final color state. The J/ψ production cross section under this model is given by [45]:

$$d\sigma(\mathrm{J}/\psi + X) = \sum_n d\hat{\sigma}(c\bar{c}[n] + X)\langle O^{\mathrm{J}/\psi}[n]\rangle, \tag{2.3}$$

where the non-relativistic QCD (NRQCD) matrix elements operators $\langle O^{\mathrm{J}/\psi}[n]\rangle$ are associated with the amplitude of producing a J/ψ from a $c\bar{c}$ pair in state $[n]$. The sizes of $\langle O^{\mathrm{J}/\psi}[n]\rangle$ parameters are determined in powers of v, the relative velocity between c and $\bar{c}$. The CSM can be restored from Equation 2.3 by keeping only the color-singlet contributions of leading order in v. At large p_{T} the J/ψ production is dominated by color octet diagrams, while the singlet color ones dominate at low p_{T} which explains the success of the CSM at low energies. Such diagrams are shown schematically in Figure 2.3.

This model has been successful in describing many charmonium observables including the J/ψ production cross sections at different LHC energies measured by ALICE as will be discussed in section 2.6.3.1. However, it fails to describe the J/ψ polarization results in $p\bar{p}$ collisions at $\sqrt{s}$ = 1.8 TeV at the Tevatron [46].

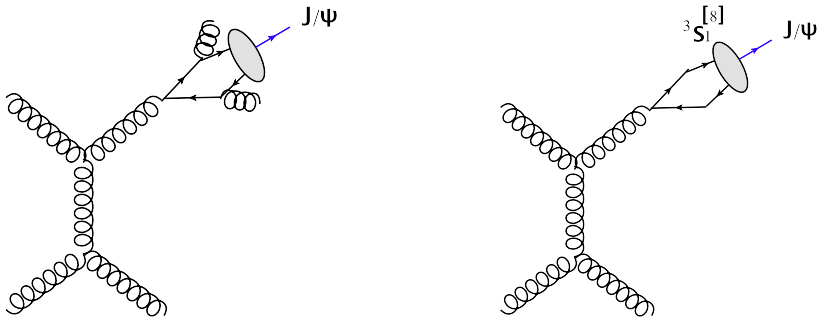

Figure 2.3: Examples of Feynman diagrams that contribute to the J/ψ production via the color singlet channel (left) and color octet channel (right) [47].

2.2.2.3 Non-prompt J/ψ production

A weak decay of a b-hadron can produce a non-prompt J/ψ as shown in the diagram of the Figure 2.4. The cross section of this process can be separated in two parts, the production of a b-hadron and its decay to a J/ψ [1]. The b-hadron cross section is theoretically factorized into two steps, perturbative one that corresponds to the b-quark production, and a non-perturbative one for the b-quark fragmentation into the hadron. The former can be evaluated using Fixed Order Next-to-Leading-Logarithm (FONLL) calculations [48], while the second one is usually extracted from e^+e^- experimental data [49].

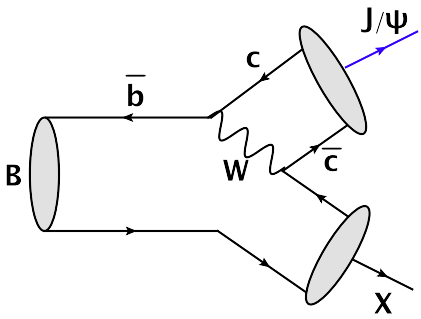

Figure 2.4: A LO contribution to the weak decay of a B hadron into a J/ψ.

2.2.3 J/ψ Photoproduction

Models and production channels discussed so far correspond all to the hadronic J/ψ production. However, photoproduction of J/ψ may also occur in nucleus-nucleus collisions due to the large involved electromagnetic field. Ultra-Peripheral Collisions (UPC), where the ions pass by each other with an impact parameter larger than the sum of their radii, allow studying the photoproduction in absence of hadronic interactions. The J/ψ production mechanism in such collisions is illustrated in Figure 2.5. One nucleus plays the role of the photon source (the photon flux grows as Z^2, where Z is the charge of the nucleus), while the other nucleus is the target. The emitted photon fluctuates into a virtual quark-antiquark pair which then interacts with the target and produce a J/ψ.
The J/ψ p_{T} spectrum is dominated by the momentum transfer from the target

nucleus since the photon p_{T} is small. A photoproduction is said to be coherent when the quark-antiquark pair interacts in phase with the entire target nucleus. In this case, the average p_{T} transfer from the target nucleus is small with a scale on the order of a few times hc/R_A [45] where R_A is the radius of the nucleus. In contrast, for the incoherent case, the quark-antiquark pair interacts out of phase so that the pair effectively interacts with a single nucleon. In this case the average p_{T} transfer corresponding to the size of a single nucleon is larger.

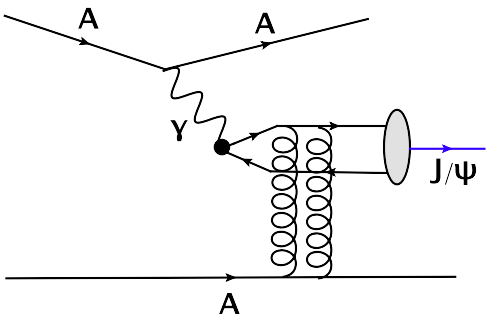

Figure 2.5: An illustration of the J/ψ photoproduction mechanism in an ultra peripheral nucleus-nucleus collision.

2.3 Cold nuclear matter effects

In this section, nuclear effects that exist even without the presence of the hot nuclear medium are discussed. Some of these effects are relevant for the production of both J/ψ and Z-boson, they will be discussed commonly. However, some of them affect only one of the probes and will be discussed within its context.

2.3.1 Nuclear parton distribution functions

Parton distribution functions (PDFs), are universal characteristics of the hadron. They are, according to the factorization theorem, the non-perturbative part of the cross sections of hard processes in hadronic collisions. They represent the probability of finding a parton with a specific flavor carrying fraction x of the hadron's longitudinal momentum at a given energy scale Q. In general, PDFs are obtained via performing global fits of different experimental datasets, using the

DGLAP evolution equation [50], [51], [52] to determine the best set of PDFs that describe the data. Experimental results included in the global fit analyses, are usually coming from Deep Inelastic Scattering (DIS) experiments. Depending on the used experimental results and the computations method, different PDF sets are available [53–55]. An example of one of them (CT14) is shown in Figure 2.6 for different partons at two different energy scales close to the mass of the charm quark and the Z-boson.

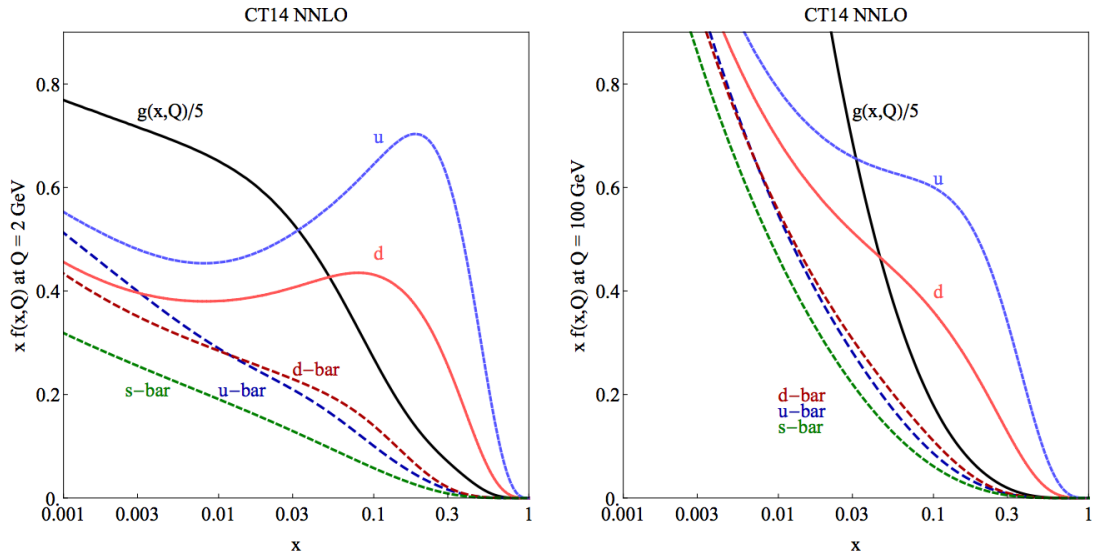

Figure 2.6: CT14 PDFs [55] for different partons (in different colors) at two different energy scales.

In 1983, the European Muon Collaboration (EMC) discovered that the partons momentum distribution in Iron (Fe) is different than the one in Deterium (De) [56] to conclude that a PDF inside a nucleus (nPDF) is different than the one in free nucleon. Since then, the phenomenon has been extensively studied, both experimentally and theoretically. The study of this subject is interesting in its own since its understanding helps to bridge the gap between nuclear and particle physics. In addition, it is crucial for other studies. In particular, precise knowledge of the nPDFs is required for predicting and understanding the results from heavy-ion collision experiments.

At a given energy scale and for a parton i that carry a fraction of longitudinal momentum x of the nucleon, the nPDF $f_i^A(x,Q^2)$ can be expressed as [57]:

$$f_i^A(x,Q^2) = R_i^A(x,Q^2) \times f_i(x,Q^2), \tag{2.4}$$

where $f_i(x,Q^2)$ is the corresponding free PDF and $R_i^A(x,Q^2)$ is its modification factor.

Similar to the free PDFs, different sets of nPDF exist [57–60]. They are also determined using global fit analyses. So far, the experimental results used in the analyses are mainly coming from lepton (charged or neutrino) DIS off nuclei, and DY production in proton-nucleus or deuteron-nucleus collisions. In contrast to the free PDFs, the nPDFs evaluation suffers from the lack of available experimental data.
Table 2.3 summarizes the characteristics of different up-to-date nPDF sets. The different sets use different free PDFs as baselines but exploit similar experimental results in their global analyses.

nPDF set	EPPS16 [61]	EPS09 [57]	DSSZ12 [58]	kA15 [59]	nCTEQ15 [60]
order in α_s	NLO	LO, NLO	NLO	NNLO	NLO
Flavor separation	Full	None	None	None	Some
Included experimental data from:					
Neutral current DIS	yes	yes	yes	yes	yes
DY dilepton $p+A/p+d$	yes	yes	yes	yes	yes
RHIC pions $d+Au/p+p$	yes	yes	yes	no	yes
Neutrino-nucleus DIS	yes	no	yes	no	no
LHC p-Pb jet data	yes	no	no	no	no
LHC p-Pb W,Z data	yes	no	no	no	no
Number of included data-points	1811	929	1579	1479	708
Number of free parameters	20	15	25	16	17
Baseline free PDFs	CT14	CTEQ6.1	MSTW2008	JR09	CTEQ6M-like

Table 2.3: Experimental status and some properties for four available nPDF sets. Table taken from [62].

A schematic illustration of a typical nPDF distribution is shown in Figure 2.7 as a function of x. One can see the different regions that correspond to different effects [63]:

- **Shadowing**: A depletion at $x \lesssim 0.1$. Usually, multiple scattering of partons in the nucleus is associated as the underlying physics explanation of this effect.

- **Antishadowing**: an excess at $0.1 \lesssim x \lesssim 0.3$. In contrast to shadowing, this can be interpreted as a result of constructive interference of amplitudes arising from the multiple scattering of partons in the nucleus.

- **EMC effect**: a depletion at $0.3 \lesssim x \lesssim 0.7$. This effect is still not totally understood. Models considering different physics processes have attempted to explain the EMC effect. These include nuclear modification of the nucleon radius and mass as well as the modification of the nucleon structure in the nuclear medium due to multi-nucleon effects (binding, pions exchange, nucleon-nucleon correlations).

- **Fermi-motion** region: an excess towards $x \to 1$ and beyond. This due to the fact that the nucleons are not stationary in the nucleus, their dynamics is known as fermi-motion.

A relevant detailed review can be found in [64].

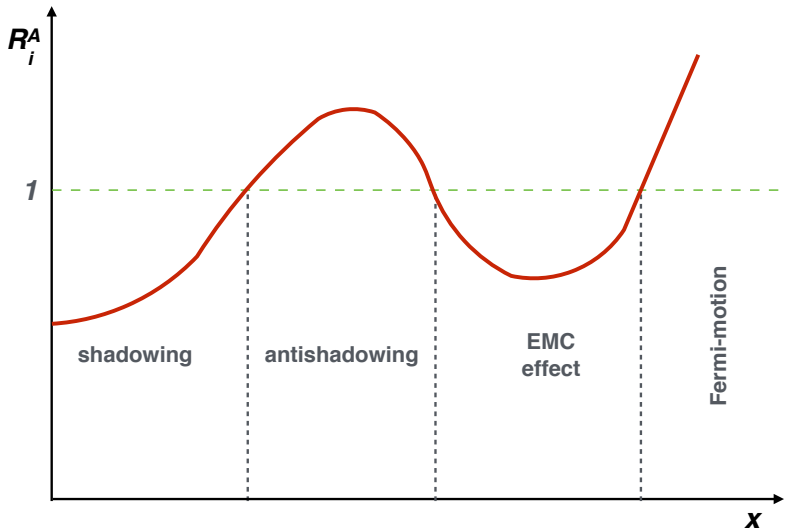

Figure 2.7: A typical nPDF distribution as a function of x [63].

As described in section 2.1 the Z-boson production at the LHC energy is dominated by the quark anti-quark annihilation process. Thus, a modification of the PDFs of the involved quarks has a direct effect on the Z-boson production.
The Z-boson production in heavy-ion collisions is considered to be a clean constraining tool of the nPDFs sets since there are no other major effects that can affect this production.
Figure 2.8 shows predictions for the modification of the Z-boson production cross section in Pb-Pb collisions with respect to pp ones at $\sqrt{s_{\mathrm{NN}}} = 5.5\,\mathrm{TeV}$, using the EPS09 parameterization [65]. One can see the potential importance of the nPDF modification effect as well as its relatively large uncertainties. This reflects the importance of measuring the Z-boson production in heavy-ion collisions.

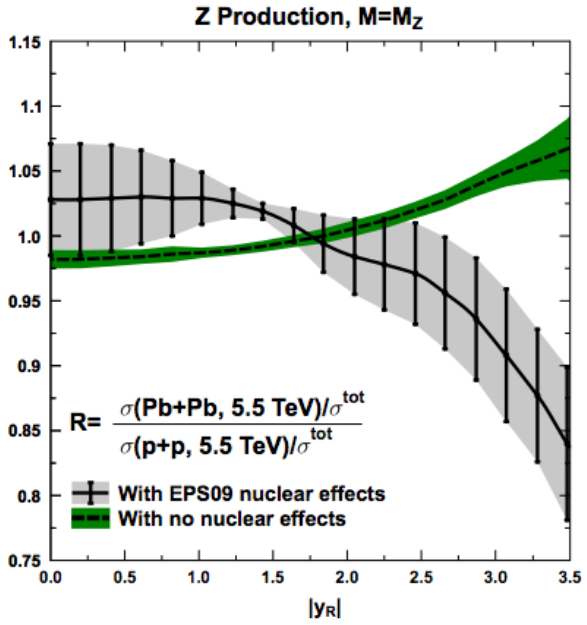

Figure 2.8: Prediction [65] for the ratio between the Z-boson cross sections in Pb-Pb and pp collisions at $\sqrt{s_{\mathrm{NN}}} = 5.5\,\mathrm{TeV}$. The effect seen on the green band is due to the isospin effect, caused by the fact that the ratio u/d quarks is not the same in nucleus than in proton.

As described in Section 2.2, the J/ψ production cross section in hadronic collisions can be factorized in two parts, where the first one is the cross section of

producing a $c\bar{c}$ pair. This cross section can be affected by the modification of the PDFs of the involved partons. Figure 2.9 shows the nuclear modification functions at the charm mass energy scale of three partons (a valence quark, a sea quark, and a gluon) in the Pb nucleus using the EPS09 parametrisation. At the LHC energy, the J/ψ production is dominated by gluon fusion, hence it is sensitive to the gluon nuclear modification function.

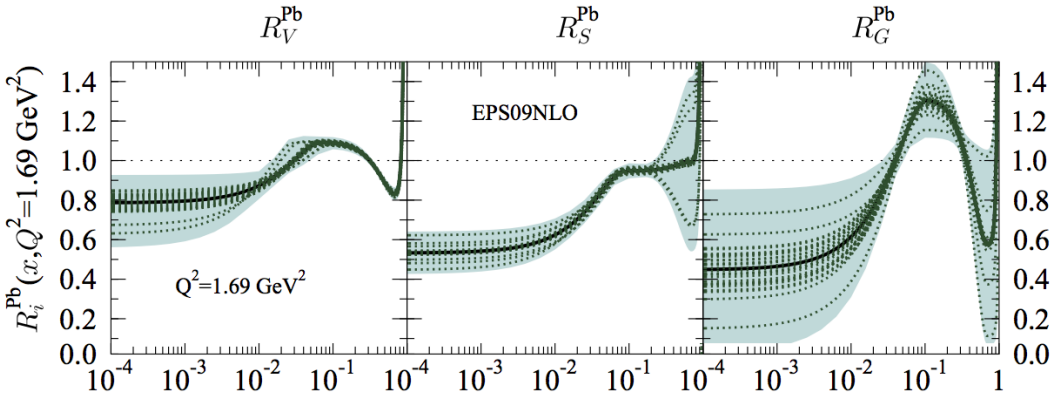

Figure 2.9: The nuclear modifications R_V, R_S, R_G for lead ion at an initial scale $Q^2 = 1.69GeV$. The thick black lines indicate the best-fit results, whereas the dotted green curves denote the error sets. Figure taken from [57].

2.3.2 Multiple scattering and energy loss

A decrease of the production cross section for a given hard probe in nuclear collisions can be caused by parton energy loss. A high energy parton traversing a nuclear medium is expected to lose energy by radiation due to multiple interactions in the target nucleus. The magnitude of this energy loss is linear with the system size L which is proportional to the nuclear size $R \sim 1.2A^{1/3}fm$ [66]. In addition to the energy loss, the incoming parton exhibits a broadeninig of its transverse momentum. This effect is known as the Cronin effect and it is also expected to be proportional to the nuclear size.

2.3.2.1 Coherent energy loss

The authors of [67] suggested that gluon radiation cannot be totally attributed to parton energy loss of a well defined parton. Indeed, at small probed x, there are some hard processes where a color charge is produced colinearly with one of the incoming partons. In such cases, gluon radiation before and after the hard process is coherent. The developed model has only one free parameter which is the transport coefficient q^0 related to the nuclear broadening and the energy loss probability distribution. Originally in Ref [67], the case of J/ψ production at forward rapidity in p-A collisions was considered since it covers small x. The c$\bar{\text{c}}$ pair is assumed to be produced in a color octet state with a time scale $\tau_{c\bar{c}}$ and travel through the nucleus for a significant time $\tau_{octet} \gg \tau_{c\bar{c}}$.
In [68], a generalized picture towards AA collisions is made.

2.3.3 Nuclear absorption

Once produced, the c$\bar{\text{c}}$ pair will traverse the nuclear matter and consequently suffer absorption both in the pre-charmonium and in the charmonium stages. This so called nuclear absorption is coming from successive interactions with the target nucleons.
When discussing the nuclear absorption of a charmonium state in the nucleus, one can compare the collision time (t_{coll}) to the formation time of the state. The former is defined as $t_{coll} = 2R\gamma_{cm}$, where R is the nucleus radius and γ_{cm} is the Lorentz factor of each of the beams in the center-of-mass frame. At the LHC energy of 2.76 TeV per nucleon, t_{coll} is expected to be less than $5 \cdot 10^{-3} fm$ [3], much smaller than the formation time of different charmonium states ($0.4fm - 1.2fm$). Therefore, one expects that the nuclear absorption plays no role at the LHC.
In p-A collisions, the authors of [69] have studied the J/ψ nuclear absorption cross section at different collision energies. This is shown in Figure 2.10 where a decreasing of the nuclear absorption cross section with increasing collision energy is seen.

[3] $\gamma_{cm} = \frac{2.76TeV}{m_p = 938MeV} \approx 2940$

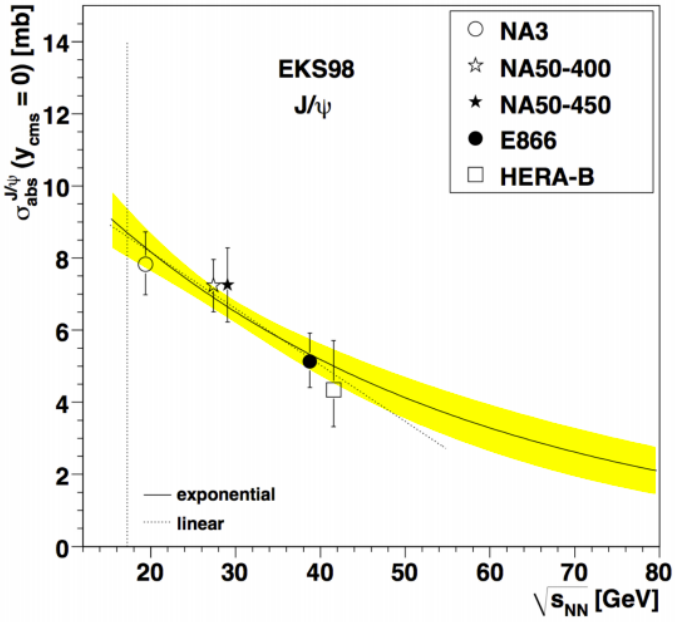

Figure 2.10: Collision energy dependence of the nuclear absorption cross section, fitted with linear and exponential function. Figure is taken from [69].

2.4 Hot nuclear matter effects on the Z-boson production

As discussed in chapter 1, a strongly interacting medium (QGP) is expected to be formed in ultra-relativistic heavy-ion collisions. In this section, induced effects on the Z-boson and its decay products are discussed.

One can see qualitatively the effects of the QGP from a timescale point of view. Indeed, due its large mass ($\sim 90\,\mathrm{GeV}/c^2$), the Z-boson formation time is very short ($\tau_Z = 1/M_Z \sim 10^{-3} fm/c$). The Z-boson decay time is inversely proportional to its width ($\sim 1/(2.5\,\mathrm{GeV}/c^2) \sim 0.08 fm/c$). On the other hand, the expected formation time of the QGP is $\sim 1 fm/c$ and it can last after a quick thermalization up to $\sim 10 fm/c$. So one expects no QGP effects on the Z-boson itself, but effects on its decay products should be accounted for.

The leptonic decay products [4] pass through the medium without strong interaction

[4] There are also the hadronic decay channels where strong interaction with the hot medium has an effect.

since they carry no color charge. However, by electromagnetic interaction with the charges of the medium, they can lose energy through elastic scatterings. This energy loss depends on the lepton mean free path estimated to be $\sim 10 fm/c$ in a T = 1 GeV medium [70] leading to an average of one elastic collision per lepton. In [71], it is shown that under such considerations, the energy loss due to lepton elastic scattering can be neglected.
This blindness of the Z-boson to the medium makes it:

- A clean constraining tool for the nPDF modifications in both nucleon-nucleus and nucleus-nucleus collisions.
- A powerful tool for validating the binary scaling of the collisions.

2.5 Hot nuclear matter effects on the J/ψ production

In this section, the various effects on the J/ψ production in nucleus-nucleus collisions were a QGP medium is created are discussed.

2.5.1 Color screening and sequential dissociation

At finite temperature, the potential in the equation 2.2 is modified due to color charge screening. This effect on the potential can be quantified by the Debye screening radius r_D. In a QGP, the quark and anti-quark of the charmonium state can no longer be bound together when the hadronic radius of the state becomes larger than r_D. Therefore a charmonium state is said to be dissociated in the QGP. The temperature at which the bound state radius, r_C, is equal to the screening length r_D, is the dissociation temperature, T_D. From the Table 2.2, one can see that the radii of the charmonium states differ, which means that some states will break up at lower temperatures than the others. Based on this picture, the authors of [72] have envisioned a hierarchy in the suppression of different charmonium states. So the observation of different charmonium states can serve as a QGP thermometer.

In order to quantitatively determine the charmonium dissociation temperature T_D in the QGP, three approaches can be followed. Two of them are based on potential models (A1, A2) and the third is based on calculation of the charmonium spectrum directly in finite temperature lattice QCD (B). In the following these approaches are described.

- (A1): at finite temperature, the potential between the quark and anti-quark becomes [73]:

$$V(r,T) = \sigma \cdot r\left(\frac{1-e^{-\mu r}}{\mu r}\right) - \frac{\alpha}{r}e^{-\mu r}, \tag{2.5}$$

  where the screening mass $\mu(T) = 1/r_D(T)$. The next step is to solve the Schrodinger equation:

$$-\frac{1}{m_c}[\nabla^2(r) + V(r,T)]\psi_i(r) = (M_i - 2m_c)\psi_i(r), \tag{2.6}$$

  where m_c is the mass of the charm quark, M_i is the mass of the charmonium state "i" and ψ_i is its wave function. With increasing temperature, the bound state "i" disappears at some $\mu^i(T) = \mu(T_D^i)$. Then this approach uses the temperature dependence of the screening mass from lattice estimations, $\mu(T) = 4T$, to determine the dissociation temperatures [74].

- (A2): the second potential model approach [75] is based on assuming that the potential $V(r,T)$ is equal to the free energy $F(r,T)$. This assumption is made by neglecting the entropy term $T\left(\frac{\partial F(r,T)}{\partial T}\right)$ in the equation:

$$V(r,T) = F(r,T) - T\left(\frac{\partial F(r,T)}{\partial T}\right). \tag{2.7}$$

  Then the dissociation temperatures are obtained by solving the Schrodinger equation using lattice QCD results for the free energy.

- (B): in this case, the spectrum $\sigma(\Omega,T)$ is calculated in the appropriate quantum channel, as a function of the temperature T and the $c\bar{c}$ energy Ω [76]. Then by changing the temperature in the performed simulations, one can obtain the dissociation temperature that corresponds to the disappearance of the charmonium bound state as illustrated in Figure 2.11.

The dissociation temperatures T_D for the different charmonium states and following the above approaches are summarized in Table 2.4.

State \ Approach	A1	A2	B
J/ψ	$\sim 1.2T_C$	$\sim 2T_C$	$1.5T_C < T_D < 2.3T_C$
ψ(2S) and χ_c	$\sim T_C$	$\sim 1.1T_C$	$T_D > 1.1T_C$

Table 2.4: Dissociation temperature T_D for different charmonium states following the different approaches described in the text of section 2.5.1.

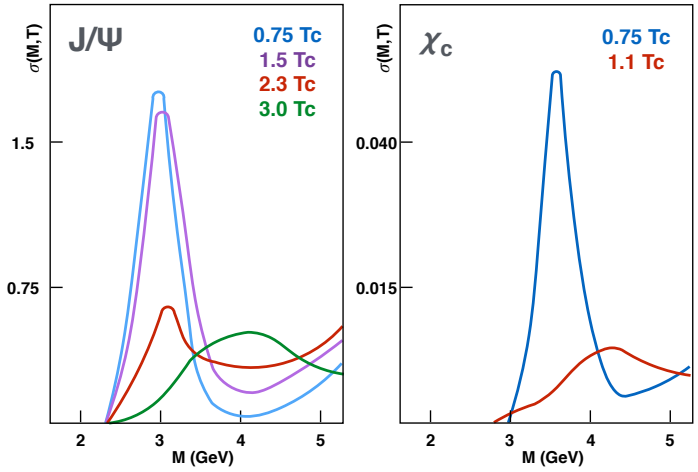

Figure 2.11: Lattice QCD simulations used for determining the dissociation temperature T_D for J/ψ (left) and χ_c (right). Figure is reproduced from [73].

2.5.2 J/ψ regeneration

At high collision energy, there is a significant number of initially produced charm and anti-charm quarks in the medium which could come close enough in phase space to form a charmonium state. This charmonium production mechanism is known as regeneration and it tends to enhance the number of observed charmonia in nucleus-nucleus collisions with respect to proton-proton collisions. The significance of this enhancement depends on the strength of the recombination between

the charm and anti-charm quarks and on the stage at which this recombination occur. Some models consider the recombination at the hadronization stage only while others consider it continuous throughout the evolution of the medium.
It is worth noting that the recombination is dominated by the initially produced charm quarks since the number of thermally produced charm quarks is too low due to the heavy mass of the charm quark.

2.5.3 Interaction with comovers

The constituents of the medium (comover particles) can scatter with the c$\bar{\text{c}}$ pair or the charmonium state (depending on their formation time compared to the charmonium one). Assuming that they interact with the c$\bar{\text{c}}$ pair, the typical reaction is $c\bar{c}+h \rightarrow D+D+X$. In this case, h stands for a comoving hadron. The probability that the bound state c$\bar{\text{c}}$ survives the interactions with comovers is given by: [77]

$$S(b) \approx exp[-\int d\tau \langle \sigma_{co} v \rangle n(\tau, b)], \tag{2.8}$$

where v is the relative velocity of the c$\bar{\text{c}}$ with respect to the comovers, $n(\tau, b)$ is the comover density at impact parameter b and time τ , and σ_{co} is the effective charmonium-comover cross section fixed from experiments at low energy. The author of [78] admits that σ_{co} could change with energy (not dramatically) but there is no possibility to determine it so they took the known one at low energy in the calculation. One can see from the equation 2.8 that with increasing energy density (i.e collision centrality) the suppression of the charmonium due to comover interaction becomes more important.

The effects from color screening, regeneration and interaction with comovers are illustrated in the cartoon of Figure 2.12 .

2.5.4 Theoretical status

In the following, a brief description of some available theoretical models that aim to describe the J/ψ production in nucleus-nucleus collisions.

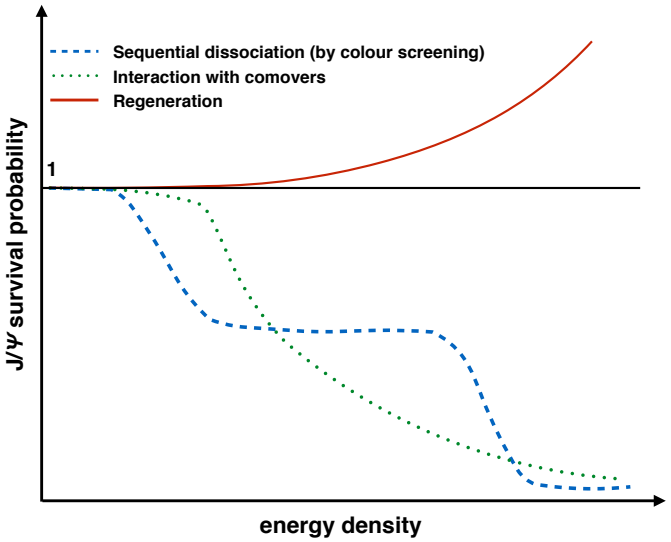

Figure 2.12: Illustration of the contribution of the color screening, interaction with comovers and regeneration to the J/ψ survival probability.

Note that other models do exist but are not described. The description is limited to the models used for the comparison with the results in chapter 6.

2.5.4.1 Statistical hadronisation model

The statistical hadronisation model was originally introduced to describe the production of hadrons with light (u, d, and s) quarks in heavy-ion collisions based on a hadro-chemical equilibrium approach [13]. This model is successful in reproducing particle ratios in a broad collision energy range (from AGS energy of ~ 10 GeV up to LHC energy). The model uses a grand canonical ensemble to describe the partition functions and hence the density of the hadrons under consideration. The only free parameters in this model are the chemical freeze out temperature and the baryo-chemical potential.
The difference with charm hadrons is that as discussed in section 2.5.2, the charm thermal rate production is negligible even at the LHC energy. Therefore, in this model, charm quarks produced in the initial hard scattering find themselves deconfined in the QGP (which means that all the produced charmonia have been color-screened). Then the charmonia and the open charm hadrons are formed

at the phase boundary according to their statistical weights (like all the other hadrons) [79, 80]. This consideration for the charm production, implies a new free parameter to the model which is the charm production cross section per rapidity unit ($d\sigma_{c\bar{c}}/dy$).
In this model all the initially produced charmonia are suppressed in the medium so the model does not include initial CNM effects on the charmonia. However, CNM effects on the $c\bar{c}$ cross section are considered.

2.5.4.2 Transport models

In models that are based on transport approach [81–83], the charmonium states (quarkonium in general) are described by the so called excitation functions f_ψ. The space-time evolution of the charmonium state in the medium is governed by the relativistic Boltzmann equation:

$$p^\mu \partial_\mu f_\psi(r,\tau,\mathbf{p}) = -E\Gamma_\psi(r,\tau,\mathbf{p}) f_\psi(r,\tau,\mathbf{p}) + E\beta_\psi(r,\tau,\mathbf{p}) \tag{2.9}$$

where τ and r are respectively the time and the spacial coordinate, while Γ_ψ and β_ψ are respectively the dissociation rate and the gain term.
In transport models, charmonia can be suppressed by inelastic scattering with constituents of the medium (light quarks, gluons or light hadrons). In QGP and for a tightly bound state (e.g charmonium) the dominant process is the gluon dissociation ($g+\psi \rightarrow c+\bar{c}+X$) [84]. In such models and in contrast to the statistical hadronisation model, charmonia are continuously suppressed and generated in the QGP. Finally, nuclear absorption, nPDF modification and Cronin effect are taken into account.

2.5.4.3 Comover Interaction Model (CIM)

As the name of the model tells, it is mainly based on the notion of interaction with comovers (section 2.5.3). This model was initially introduced in [85] as an alternative to the color screening mechanism in describing the anomalous charmonium suppression observed at SPS [86]. As for the transport models, the CIM is also based on rate equations, but the difference is that the CIM does not assume a QGP formation and hence medium equilibrium.

While the first version of the model [85] does not take charmonium regeneration into account, it was included as a gain term in the rate equations in a revisited version of the model [78].
Finally, the CIM takes into account nuclear shadowing which is calculated within the Glauber-Gribov model [87].

In the early versions of the model [85], the comover medium was considered to be only hadronic and no charmonium regeneration was taken into account. However, in a revisited version of the model [78], partonic comoving medium was also considered and the regeneration was also included as a gain term in the rate equations.

2.6 Experimental results

In this section, experimental results that are related to the subjects of this manuscript will be summarized.

2.6.1 Z-boson production in heavy-ion collisions

The Z-boson production measurement in heavy-ion collisions has only become accessible at the LHC thanks to the large center of mass energies and available luminosities. chapter 5 will present the results of this production in p-Pb and Pb-Pb collisions at $\sqrt{s_{\mathrm{NN}}} = 2.76\,\mathrm{TeV}$, measure by the ALICE detector. Below, a summary of the results of this production measure dby different experiments in different collision systems:

2.6.1.1 Pb-Pb at $\sqrt{s_{\mathrm{NN}}} = 2.76\,\mathrm{TeV}$

The first Z-boson production measurement in heavy-ion collisions corresponds to Pb-Pb collisions at $\sqrt{s_{\mathrm{NN}}} = 2.76\,\mathrm{TeV}$. The Z-boson yield measured by ATLAS [88] (Figure 2.13 left), is compared to model calculation using PYTHIA [89]. The model takes into account the isospin effect but it does not account for the nPDF modifications. One can see that within uncertainties, the data are well reproduced by this model.

In addition to the Z-boson yield, CMS has measured the nuclear modification factor R_{AA}[5] [90] which is the yield observed in nucleus-nucleus collisions relative to the one in pp collisions scaled by the number of binary nucleon-nucleon collisions (N_{coll}) as shown in Figure 2.13 right. In the calculation of R_{AA}, the Z-boson pp cross section is measured at the same energy. One can see from the flat behavior of the R_{AA} centrality dependence, within uncertainties, that the production cross section scales with the number of nucleon-nucleon collisions.

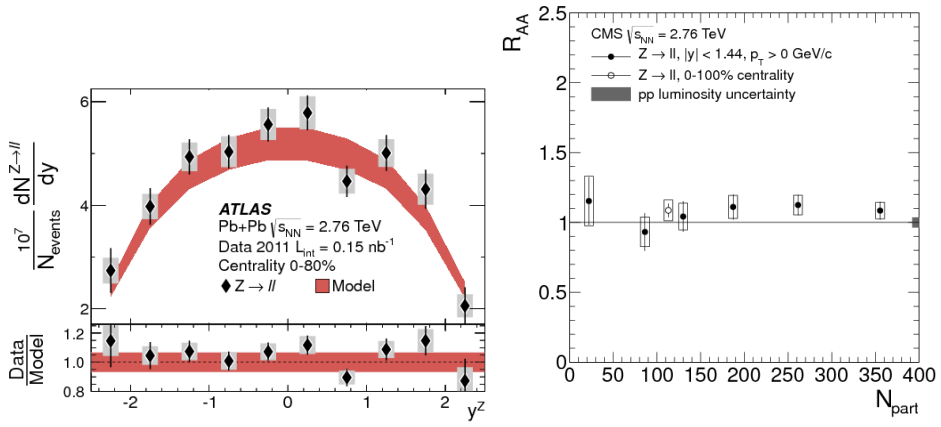

Figure 2.13: Left: Z-boson yield measured by ATLAS [88] in rapidity bins and compared to prediction based on PYTHIA. Right: Z-boson R_{AA} vs the collision centrality measured by CMS [90]. Both measurements are performed in Pb-Pb collisions at $\sqrt{s_{\mathrm{NN}}} = 2.76\,\mathrm{TeV}$.

2.6.1.2 p-Pb at $\sqrt{s_{\mathrm{NN}}} = 5.02\,\mathrm{TeV}$

In this collision system, the Z-boson production has been measured by the four LHC experiments. At mid-rapidity, ATLAS [91] and CMS [92] have measured it in the leptonic (combined electronic and muonic) decay channel. In Figure 2.14, the measured cross section results are compared to theoretical calculations, both with and without including nPDFs modification. Within uncertainties, both set of models are able to describe the data.
These results (among others) have been recently added to the global fit analysis by

[5]Defined in chapter 4

the EPS09 group, leading to an updated nPDF set EPPS16 [61].
At forward rapidity, the LHCb experiment has measured the Z-boson production in the dimuon decay channel [93]. Figure 2.15 shows the cross section results in two center-of-mass rapidity regions, also compared to theoretical calculation with and without including of nPDF modification. With the large statistical uncertainties, a clear conclusion could not be drawn on whether or not the agreement between the data and the theory is better with including of the modifications of nPDF.

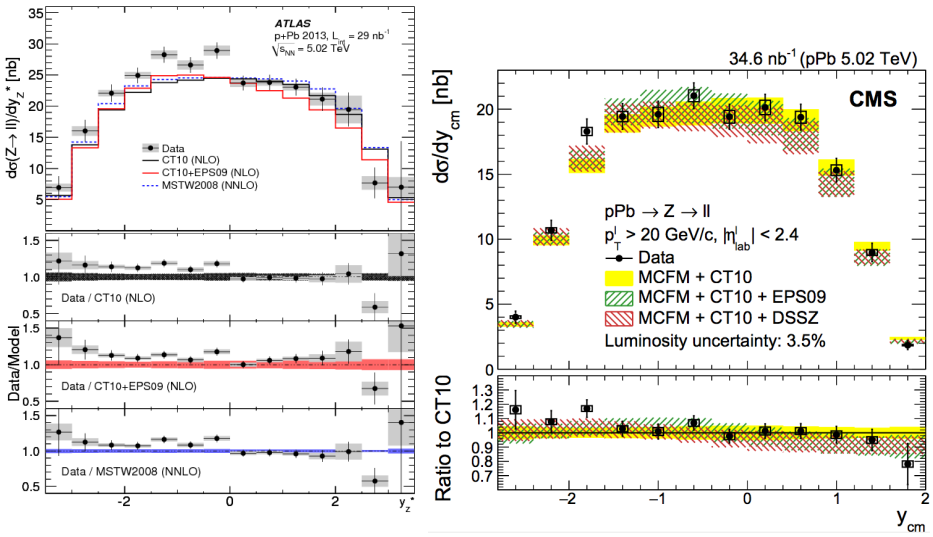

Figure 2.14: Left (right): the Z-boson cross section in p-Pb collisions measured by ATLAS [91] (CMS [92]) and compared to models with and without accounting for nPDF modification.

2.6.2 J/ψ production in heavy-ion collisions

2.6.2.1 At SPS

Nine years after the original prediction of the J/ψ suppression, the NA50 experiment at the SPS (CERN) measured the J/ψ production in Pb(158 AGeV)-Pb

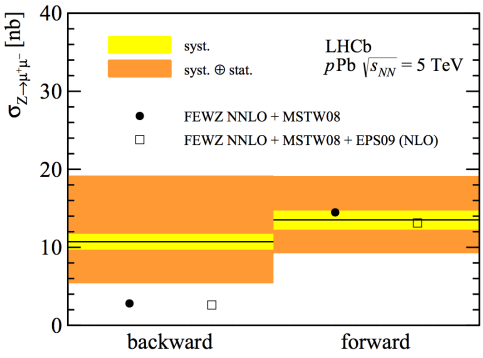

Figure 2.15: Z-boson cross section in p-Pb collisions measured by LHCb and compared to models with and without accounting for nPDF modification [93].

collisions [6] [86]. The suppression was quantified using the J/ψ to Drell-Yan (DY) ratio since the DY production is not affected by the presence of the hot medium or by nuclear absorption. As shown in the Figure 2.16, the J/ψ suppression was found to be stronger than the one predicted by only nuclear absorption based on a Glauber model. Because of the deviation from the nuclear absorption prediction, the suppression was called "anomalous" and the NA50 experiment concluded in [94] that this suppression provides an evidence for the de-confinement of quarks and gluons in heavy-ion collisions.

2.6.2.2 At RHIC

Six years after the J/ψ anomalous suppression reported by NA50, RHIC provided the first J/ψ data in Au-Au collisions at a center of mass energy of 200 GeV [95]. The R_{AA} was introduced to quantify the J/ψ suppression. Figure 2.17 shows the comparison of the J/ψ suppression observed at SPS and RHIC in terms of an R_{AA} corrected by the CNM effects which are important at the two energies. Despite the factor of 10 higher collision energy at RHIC, the magnitude of the anomalous suppression is similar which is not expected in the picture of color screening alone. However, theoretical models that include the J/ψ regeneration component [79, 83], [96, 97] (see section 2.5.2) had anticipated a weaker J/ψ suppression at RHIC

[6] This corresponds to ~ 17 GeV of energy in the center of mass

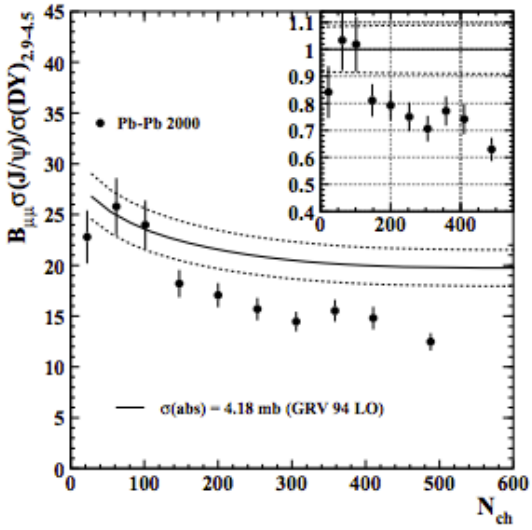

Figure 2.16: The ratio between the J/ψ and DY cross sections in Pb(158 AGeV)-Pb collisions at the SPS, measured by the NA50 experiment [86]. The dotted band corresponds to the prediction based on nuclear absorption

compared to what is predicted by color screening melting alone. This is based on the fact that the regeneration component becomes more important at RHIC due to the increase of the collision energy. Additional support for the necessity of including the regeneration component arose from the observation that J/ψ suppression at RHIC is less pronounced at mid rapidity relative to forward rapidity as shown in 2.17. It was argued that dissociation by color screening should be higher at mid-rapidity due to the larger energy density. However, this is compensated by the increasing J/ψ enhancement by regeneration at mid-rapidity due to larger charm production cross section.

2.6.2.3 At LHC

To shed light on the complexity of charmonium suppression and regeneration mechanisms in nucleus-nucleus collisions, the J/ψ production has been measured in Pb-Pb collisions, at two different center-of-mass energies $\sqrt{s_{\mathrm{NN}}} = 2.76\,\mathrm{TeV}$ and $\sqrt{s_{\mathrm{NN}}} = 5.02\,\mathrm{TeV}$. The latter is one of the main subjects of this manuscript and will be discussed in details in chapter 4 and chapter 6.

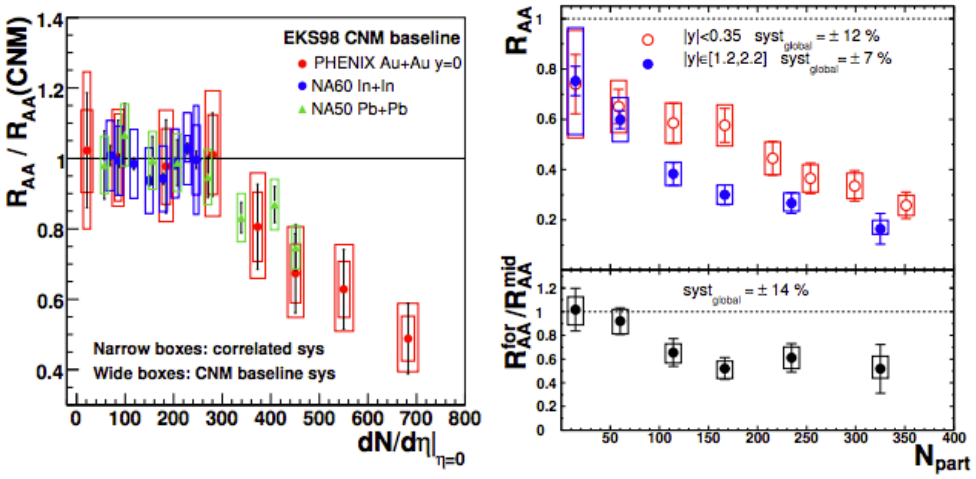

Figure 2.17: Left: the comparison between the J/ψ nuclear modification factor measured at SPS [94] and RHIC [95] (Figure taken from [45]). Right: the J/ψ R_{AA} measured at RHIC by PHENIX in two rapidity regions [95]

2.6.3 J/ψ production in small systems

In this manuscript, the focus is on the J/ψ production in Pb-Pb collisions which addresses the understanding of hot nuclear effects. However, the J/ψ production in smaller collisions systems have been studied for different motivations. In the following, some results on the J/ψ production in pp and p-Pb collisions are presented. The presentation is limited to measurements by ALICE at the LHC but results on the same topics by other LHC experiments and outside the LHC also exist.

2.6.3.1 J/ψ production in pp collisions

The study of the J/ψ production in pp collisions has two main motivations:

- A baseline for measurements of J/ψ production in heavy-ion collisions since no hot or cold nuclear effects are expected in pp collisions.
- Essential to understand the J/ψ hadronic production mechanisms.

ALICE has measured the J/ψ production in pp collisions at the different center-of-mass energies provided by the LHC (2.76, 5.02, 7, 8, and 13 TeV). Figure 2.17

shows the rapidity and p_{T} differential cross sections of inclusive J/ψ production at these energies. In [98], these cross sections were found in agreement with theoretical NRQCD calculations [44].
In chapter 4, more details will be presented on the J/ψ production cross section in pp collisions at $\sqrt{s}$ = 5.02 TeV since it will be used as a reference for the J/ψ production in Pb-Pb collisions.

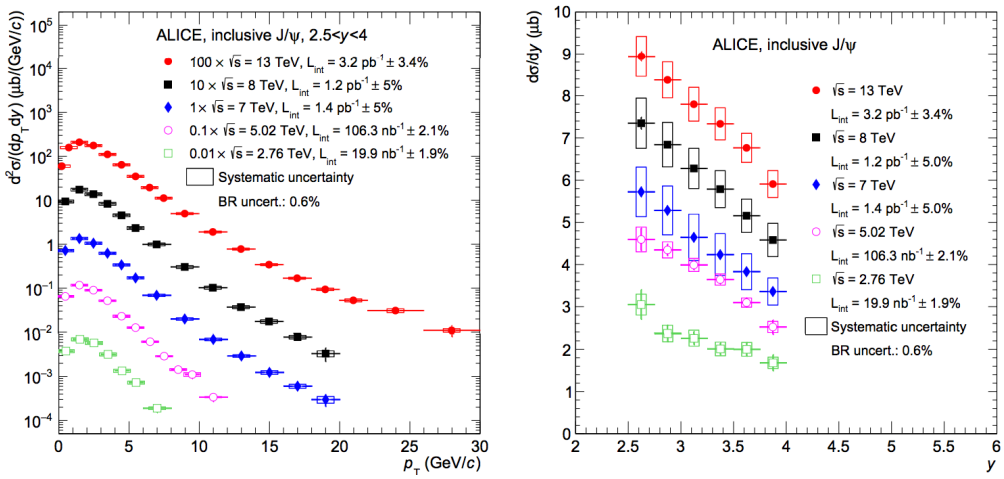

Figure 2.18: Left (right) panel: the J/ψ production cross section in pp collisions at different center-of-mass energies as a function of p_{T} (rapidity) measured by ALICE [98].

2.6.3.2 J/ψ production in p-Pb collisions

Hot nuclear effects are not expected to take place in p-Pb collisions. Therefore, measuring the J/ψ production in these collisions allows to quantify the cold nuclear matter effects on this production. To this date, the LHC has provided p-Pb collisions at two different center-of-mass energies, 5.02 and 8.16 TeV. At both energies, different J/ψ measurements were done. The J/ψ nuclear modification factor in p-Pb collisions (R_{pPb}) quantifies the J/ψ suppression in p-Pb collisions with respect to pp collisions. Figure 2.19 shows the R_{pPb} at $\sqrt{s_{\mathrm{NN}}}$ = 5.02 TeV as a function of rapidity. In the positive rapidity region (which probes the small Bjorken-x of the Pb ion), the measured J/ψ suppression is clear. This shows that the size of CNM effects is not negligible on the J/ψ production in heavy-ion collisions. Within uncertainties,R_{pPb}

is in agreement with theoretical calculations based on nuclear shadowing using the EPS09 parametrization [57] and coherent energy loss [67].

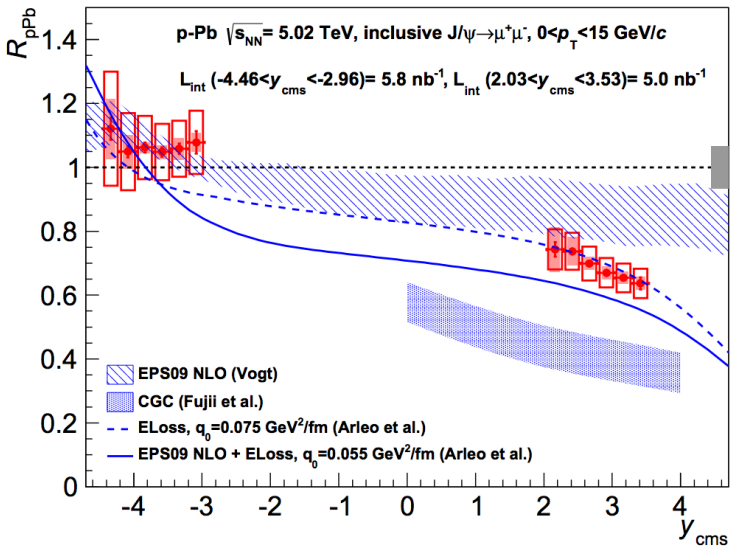

Figure 2.19: J/ψ nuclear modification factor in p-Pb collisions at $\sqrt{s_{\mathrm{NN}}} = 5.02\,\mathrm{TeV}$ measured by ALICE and compared to different theoretical calculations [99].